ACS OMEGA

http://pubs.acs.org/journal/acsodf

Article

Optimization of Colloidal Gold Nanoparticles on Porous Anodic Aluminum Oxide Substrates for Refractometric Sensing

Uldis Malinovskis, Raimonds Popļausks, Aušrinė Jurkevičiūtė, Aleksandrs Dutovs, Karlis Berzins, Vladislavs Perkanuks, Wojciech Simka, Indrikis Muiznieks, Donats Erts, and Juris Prikulis*

Cite This: *ACS Omega* 2022, 7, 40324−40332

Read Online

ACCESS | Metrics & More | Article Recommendations | Supporting Information

ABSTRACT: A new composite metal−insulator−metal (MIM) system consisting of exceptionally dense non-close-packed (NCP) arrays of gold or silver nanoparticles, porous anodic aluminum oxide (PAAO), and bulk aluminum substrate interacts strongly with visible light and may become a very useful component for optical applications. The proposed MIM structure can be synthesized using accessible lithography-free chemical and physical processes (anodization and capillary force assisted colloidal particle deposition) that are suitable for the low-cost production of specialized devices. Here, we present a systematic study to determine the essential MIM structure parameters (nanoparticle size and PAAO layer thickness) for localized surface plasmon resonance (LSPR) refractometric sensing. A performance comparison was done by recording the spectra of scattered light upon angled illumination in media with different refractive indices. A clear advantage for maximizing the signal to background ratio was observed in the case of 60 and 80 nm Au nanoparticles with a PAAO thickness in a narrow range between 300 and 375 nm. Sensitivity exceeding a 200 nm peak wavelength shift per refractive index unit was found for 60 nm Au nanoparticles on approximately 500-nm-thick PAAO. The experimental observations were supported by finite-difference time-domain (FDTD) simulations.

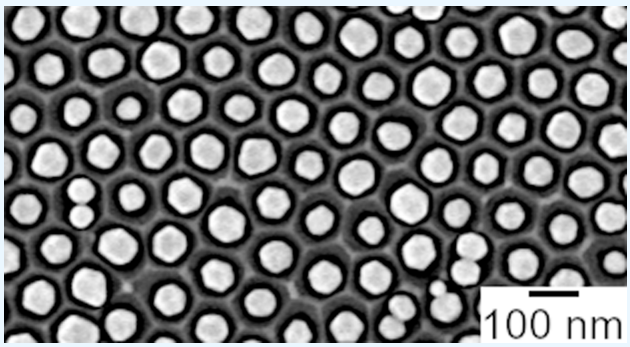

1. INTRODUCTION

Application of metal nanoparticles for refractometric sensing using localized surface plasmon resonance (LSPR) has been an active research area for several decades.[1] The presence of the analyte can conveniently be detected as a shift of resonance wavelength or change of the peak intensity using various optical configurations, such as extinction, reflection, or dark-field setups. However, a widespread use of LSPR sensors has been hindered by the technological difficulties to produce reliable, low-cost nanostructured substrates. A potential solution for scalable production of suitable surfaces could be based on self-organized materials such as porous anodic aluminum oxide (PAAO).[2] The PAAO pores can be grown as straight channels with a local hexagonal or short-range ordering.[3] Capillary force assisted (CFA) colloidal nanoparticle array (NPA) deposition on PAAO is a new, not fully explored technique that uses a type of guided self-assembly to produce NPA without nanolithography or other advanced manufacturing methods.[4]

Since the first report on the application of PAAO templates for CFA deposition,[4] the technique has been refined to achieve highly uniform arrays of monodisperse non-close-packed (NCP) arrays of metal nanoparticles for use as surface-enhanced Raman scattering (SERS) and LSPR sensor substrates,[5] construction of surfaces with controlled reflectance,[6] as well as second-harmonic generation.[7] CFA colloidal particle deposition on PAAO can potentially resolve the technological difficulties of LSPR sensor substrate production since it is a very accessible method that can be applied in a standard wet chemistry lab. The technology does not require a vacuum, extreme temperatures, exotic materials, or highly specialized equipment. A further advantage is that no adhesive layer is needed for metal nanoparticles, which could deteriorate the plasmon resonances.[8] PAAO templates can host non-metallic NCP arrays as well, including silica[9] and diamond.[4]

PAAO is a highly versatile material[2] with many well-known synthesis methods, which enable tuning of pore diameters and interpore distances.[10] Upon application of the anodizing voltage, the Al^{3+} ions and the oxygen containing ions (O^{2-} and OH^{-}) migrate through the barrier layer.[11] These ions in reactions with aluminum in the acidic electrolyte lead to the

Received: August 18, 2022
Accepted: October 14, 2022
Published: October 28, 2022

https://doi.org/10.1021/acsomega.2c05305
ACS Omega 2022, 7, 40324−40332

formation of amorphous oxide film.[10] In a steady state process, new Al_2O_3 is formed at the metal−oxide interface and compressed into solid pore walls due to increased volume. Figure 1a shows a cross-section of a typical PAAO layer that

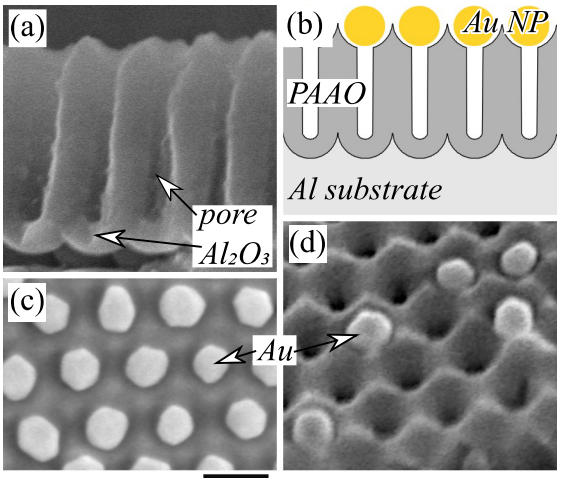

Figure 1. (a) Scanning electron microscope (SEM) image of PAAO cross-section. (b) Schematic illustration of sample structure. (c) Top view SEM image of 60 nm diameter Au nanoparticle NCP array. (d) Tilted view SEM image of sparse 60 nm diameter Au nanoparticles on PAAO. Scale bar 100 nm for all SEM images.

was produced using one of the most popular anodization protocols in 0.3 M $H_2C_2O_4$ (oxalic acid) electrolyte and 40 V anodizing potential. The actual system under investigation in the present study is a composite multilayered (sandwich) structure (Figure 1b), which consists of a bulk aluminum substrate, a variable thickness porous PAAO layer, and an NCP array of Au nanoparticles with different diameters.

In this study, we analyzed the influence of PAAO layer thickness on LSPR sensing properties by various sized Au nanoparticles. The performance comparison was based on bulk refractive index sensitivity,[12] which is a critical parameter for practical sensor applications. In previous research on similar structures, a moderate refractive index (RI) sensitivity (<75 nm/RIU) was reported;[5] however, the PAAO thickness selection was in a very narrow interval. Interestingly, no LSPR scattering peaks could be found for 40 nm diameter Au NPA. As will be shown, the LSPR scattering can be significantly enhanced with a proper selection of PAAO layer thickness. We also demonstrate, how the distance between the NPA and Al substrate affects the RI sensitivity and figure of merit (FoM).

Although higher RI sensitivity can be expected for more complex nanoparticle shapes, such as nanobranches[13] or prolate nanoparticles with a high aspect ratio,[14] we used the well-defined monodisperse spherical nanoparticles to illustrate the underlying physical phenomena and simplify modeling.

2. RESULTS AND DISCUSSION

When a simple dip-coating setup was used at slow withdrawal speeds (0.1 μm/s), sufficiently large NPA regions with nearly 100% loading density (Figure 1c and Supporting Information (SI) Figure S1) could be produced. Due to repetitive stretching and rupture of the meniscus during convective self-assembly of colloidal nanoparticles,[15] the high-density regions form a stripe pattern that can be resolved optically. At high withdrawal speeds, sparse NP could be deposited on the PAAO without aggregation. All individual NPs are preferably located in the funnels above PAAO pores (Figure 1d). Under angled illumination (Figure 2), bright and colorful scattering

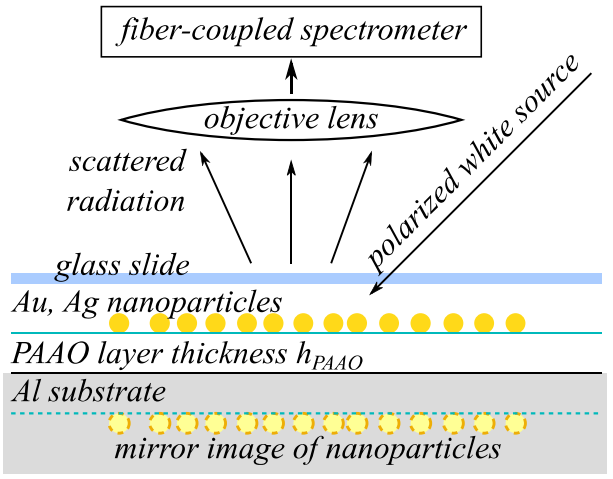

Figure 2. Schematic of the optical setup (not to scale).

could be observed by the naked eye (Figure S2). Sample coloring and intensity depended on the PAAO layer thickness, which indicated the possibility to optimize potential optical sensor devices for specific wavelengths. However, the anodic aluminum oxide is not a homogeneous material but consists of an Al_2O_3 barrier layer, a porous layer, and a layer with funnel-shaped pore openings. Therefore, we introduce an effective PAAO layer thickness h_{PAAO}, which is directly related to the optical properties of the alumina film and provides an estimate of the geometric cross-section. In order to establish the basic relationship between the scattering properties and PAAO layer thickness, spectra were recorded from a sparse 60 nm diameter Au NP on PAAO that was synthesized on single crystal aluminum substrates. This eliminated the PAAO thickness variation, which arises on polycrystalline materials (rolled sheets) due to different electrochemical reaction rates on aluminum grains with different crystallographic orientations.[16] The low loading density in this case minimized any spectral changes due to electromagnetic coupling between particles that could be significant in high-density arrays.[17] In the narrow range of h_{PAAO} near 300 nm, the sparse NP showed several important spectral properties (Figure 3a) that were used as a guide for subsequent studies of high density NPA: (i) The peak wavelength λ_{max} dependence on h_{PAAO} could be satisfactory approximated by a linear function (Figure 3b and Figure 4b as will be discussed later). (ii) The maximum scattering efficiency Q_{max} showed a nonmonotonous dependence on h_{PAAO} with an apparent maximum near 280 nm (Figure 3c). (iii) Despite a relatively big variation in scattering intensity (approximately 20%), which can be caused by the different loading densities at randomly selected spots, the peak wavelength remained fixed within a few-nanometer interval at any given PAAO layer thickness. (iv) TE or s-polarized illumination typically resulted in higher scattered signal intensity and more symmetric spectral peaks. This can be understood since upon s-polarized excitation all induced nanoparticle dipoles oscillate in the same mode parallel to the sample surface. However, for the p-polarized excitation, there is an additional component, which is normal to the

https://doi.org/10.1021/acsomega.2c05305
ACS Omega 2022, 7, 40324−40332

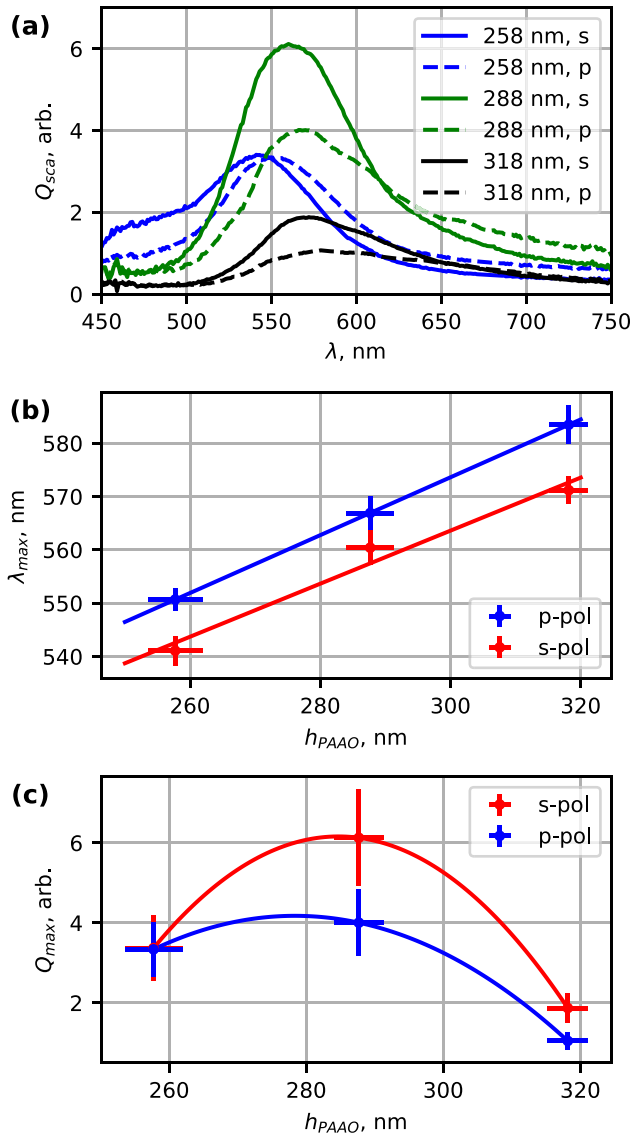

Figure 3. (a) Averaged scattering efficiency spectra by 60 nm Au nanoparticles on various thickness (258 nm, 288 nm, 318 nm) PAAO layers on single crystal <100> aluminum substrates recorded using 60° incidence angle illumination with transverse-electric (TE, s) and transverse-magnetic (TM, p) polarization. (b) Dependence of scattering peak wavelength λ_{max} on PAAO layer thickness. (c) Dependence of scattering peak value on PAAO layer thickness. Error bars show standard deviation of measurements at different spots on the same single crystal substrate.

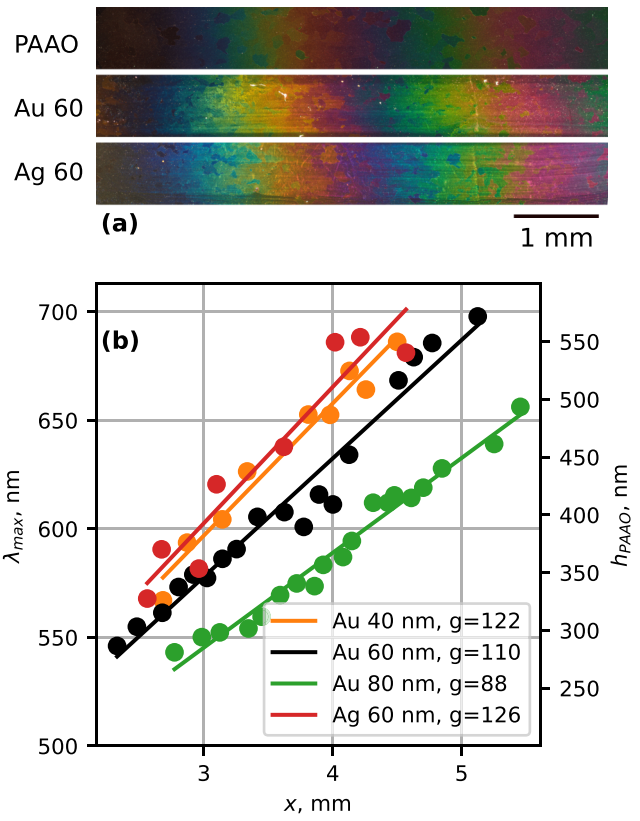

Figure 4. (a) Dark-field photomicrographs of variable thickness Al-PAAO and Al-PAAO after dip-coating in 60-nm-diameter Au and Ag colloids. (b) Dependence of scattering peak wavelength on sample lateral coordinate x. Legends indicate the nanoparticle material, diameter and estimated thickness gradient $g = \Delta h_{PAAO}/\Delta x$ in nm/mm units.

sample surface with a different resonance and radiation pattern.[18]

For the s-polarized illumination in air, a relationship $h_{PAAO} = 2.01\lambda_{max} - 833$ nm was established as a convenient and nondestructive method to estimate the h_{PAAO} without the use of SEM measurements of the cross-section. It should be noted that this linear relationship is specific to the particular optical setup and may depend on the angle of incidence and uncertainty of the effective refractive index of PAAO, where huge variations have been reported.[19] High-density NPA would also have slightly red-shifted $Q_{sca}(\lambda)$ peaks (~tenths nm). Nevertheless, the linear approximation is an important step for practical sensor substrate optimization, where optical-only measurements are desired to control the peak wavelength, without actually probing the geometric layer thickness. Such simplification was justified by the observations on PAAO with a constant thickness-gradient $g = \Delta h_{PAAO}/\Delta x$. As can be seen in Figure 4a, the sample colors were primarily determined by the thin-film interference (TFI) in the PAAO layer, but the presence of Au and Ag nanoparticles increased the image brightness without a major impact on apparent colors. However, the relative intensities of each color component were different depending on the nanoparticle size and material (Figure S2). The linear dependence between λ_{max} and h_{PAAO} was confirmed in the thickness range ~300 nm to 600 nm by linear relation between λ_{max} and the lateral sample coordinate x on constant-gradient specimens (Figure 4b).

Figure 5 shows an example analysis of a single spot that was measured on a 60 nm diameter Au NCP array on variable thickness PAAO. There is a notable color change in the dark-filled micrographs (Figure 5a,b,c) taken in media with different RI values. Within each photomicrograph, a grain boundary in underlying aluminum substrate can be seen as a sharp border that separates regions with distinct colors. This is caused by different electrochemical reaction rates on aluminum grains with different crystallographic orientations,[16] which results in different PAAO thicknesses using constant anodization time. The RI sensitivity can be observed in the scattering spectra (Figure 5d) as a red-shift of the peak wavelength with increasing RI value (Figure 5e). More examples of scattering spectra in different RI media are available in the Supporting Information (Figure S3). Scattering spectra from a reference

https://doi.org/10.1021/acsomega.2c05305
ACS Omega 2022, 7, 40324−40332

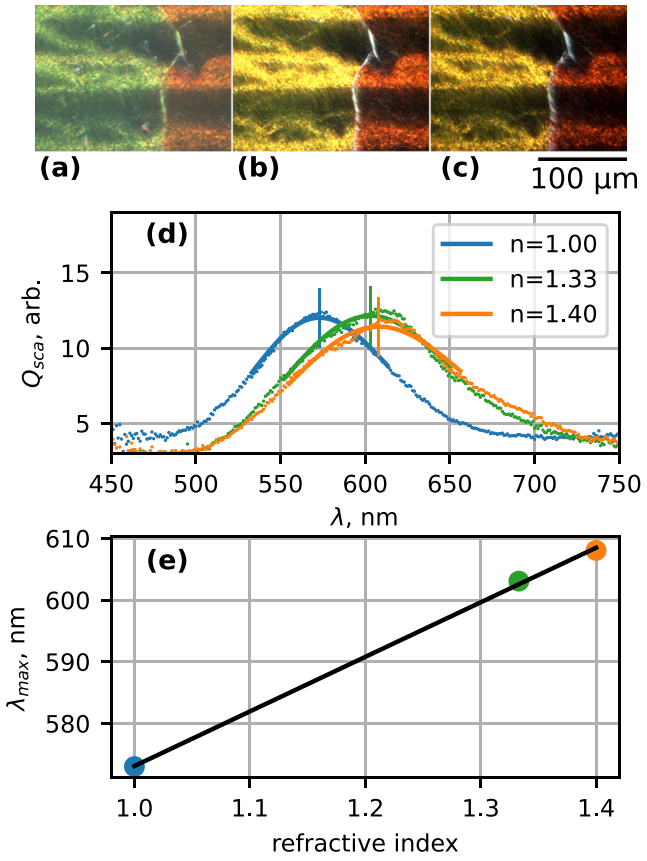

Figure 5. Photomicrographs of an Al-PAAO-NPA (60 nm Au particle diameter) sample in media with different refractive indexes: (a) air, n = 1.00; (b) water, n = 1.33; (c) sucrose solution, n = 1.40. The estimated h_{PAAO} of the green/yellow/orange grain (on the left of each micrograph) is 320 nm. (d) Recorded scattering spectra from the grain in different media. Solid lines show a segment of polynomial fit between inflection points that are used as the FWHM value for the scattering peak. Vertical markers show the peak wavelength as determined from polynomial fit. (e) Dependence of the scattering peak wavelength on media refractive index.

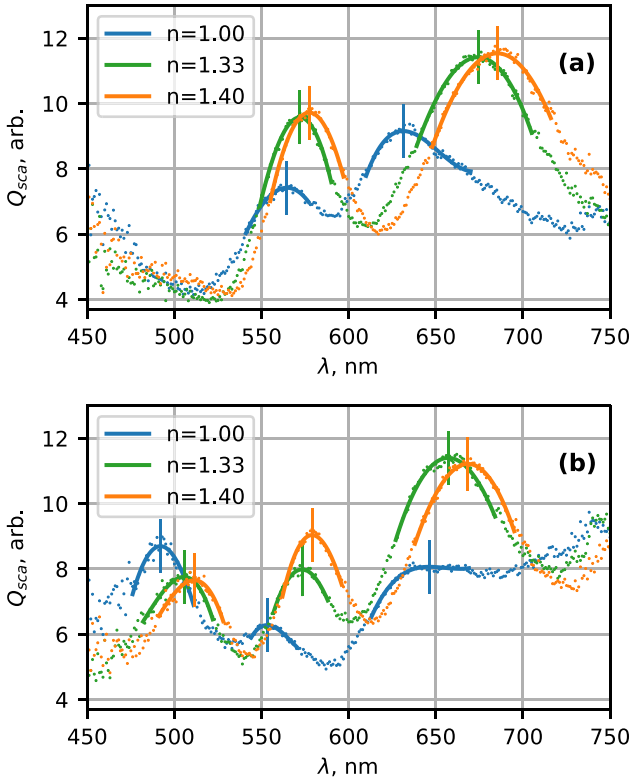

Figure 6. Scattering spectra of 80-nm-diameter Au NP on Al-PAAO in different media recorded at spots with estimated thickness: (a) 909 nm and (b) 1032 nm.

PAAO sample without any nanoparticles are shown in Figure S5. Such spot analysis was done on multiple locations with different thicknesses on each variable-thickness sample and repeated on samples with different Au NP diameters (40 nm, 60 nm, 80 nm) and a 60 nm diameter Ag NP sample for comparison. In the peak wavelength range (550−700 nm) or corresponding thickness range (275−575 nm), the scattering maxima could be clearly identified and peak widths measured. For spots with thinner PAAO (below ∼275 nm) the scattering was very weak and peaks could not be found above the noise and background. This can be also seen in photomicrographs in Figure 4a, where the thinner parts of the sample (left side of each stripe) appear dark. For thicker PAAO, the main peak shifted toward infrared and new higher order peaks appeared in the visible range as exemplified by scattering spectra from 80 nm diameter Au NP on ∼1-μm-thick PAAO layer (Figure 6a,b). Notably, in comparison to the first order scattering peaks (Figure 5d), the higher order peaks (Figure 6) were significantly narrower and in the 650−700 nm wavelength range showed higher sensitivity $\Delta\lambda/\Delta n$. This indicates that the higher order peaks can potentially be used for RI sensing with a better figure of merit (FoM). However, for 40 and 60 nm diameter Au NP, the higher order peaks were asymmetrical, overlapping, and hidden in the background, which complicated the data processing for sensor readout.

In the following, we limit the analysis to the first order scattering peaks only. The results are summarized in Figure 7, but a separate series with more data points for 60-nm-diameter Au NP is presented in Figure S4. At h_{PAAO} < 400 nm, the refractive index sensitivity $S = \Delta\lambda/\Delta n$ (Figure 7a) was close to 75 nm/RIU for all Au nanoparticles, similar to a previous report[5] with a tendency to increase to 100 nm/RIU and above for higher PAAO thickness. However, in the case of 60 nm Au particles, S had a maximum, exceeding 200 nm/RIU at h_{PAAO} = 500 nm. Figure S4b shows similar behavior, but an additional sensitivity peak appeared at λ_{max} = 600 nm, which corresponds to 370 nm effective PAAO thickness. This may be caused by a different size and shape distribution of the particular batch of colloid or differences in the optical setup and numerical aperture of the objective lens. Nevertheless, sensitivity values above 200 nm/RIU can be found at certain PAAO thickness intervals. For comparison, similar samples with 60 nm Ag NPA had an average value of S just below 200 nm/RIU and within the explored PAAO thickness range did not show a clear improvement with variation of h_{PAAO}. According to Mie theory simulations,[14] Ag particles should generally have higher RI sensitivity than Au particles with the same size. The figure of merit (Figure 7b) shows similar behavior to sensitivity because the peak widths (Figure 7d) have little variation (within approximately 20%) depending on h_{PAAO}. The obtained FoM in the 0.5−2.5 range for Au NP are comparable to measurements using single nanoparticles[12] where values in 1−2.5 range have been reported. A further comparison can be made to RI sensitivity of single 70 nm diameter gold nanospheres (78.9 nm/RIU) and their dimers (187.8 nm/

https://doi.org/10.1021/acsomega.2c05305
ACS Omega 2022, 7, 40324−40332

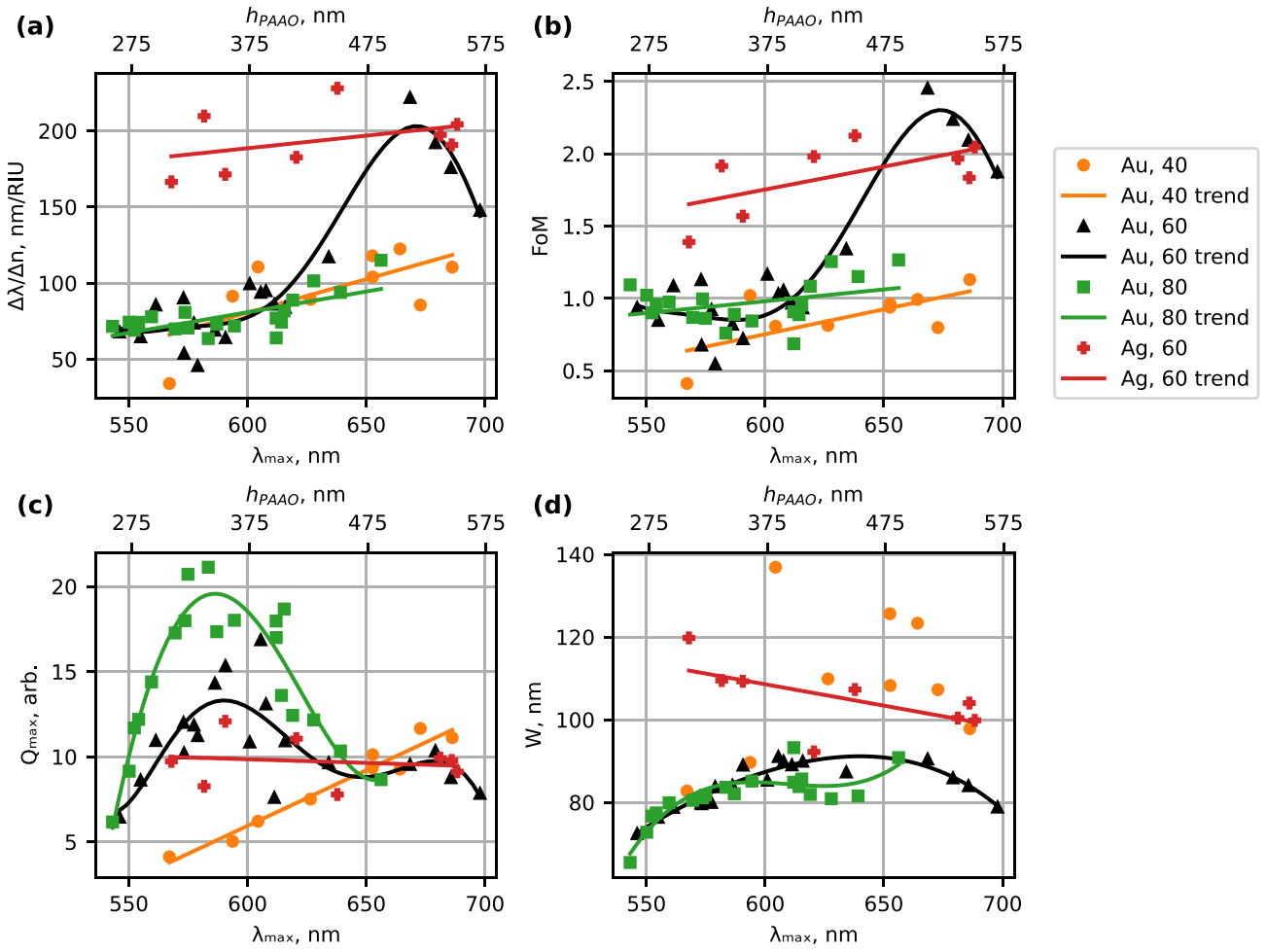

Figure 7. Summary of sensor performance parameters measured at different effective PAAO layer thicknesses h_{PAAO} and corresponding scattering peak wavelength λ_{max}: (a) refractive index sensitivity, (b) figure of merit, (c) peak scattering efficiency, and (d) peak width (difference between inflection points).

RIU).[20] For 35 nm × 75 nm Au nanorod 1D arrays with 25 nm gaps that were produced using electron beam lithography, experimental (140 nm/RIU) and simulated (201 nm/RIU) values were reported.[21] Thus, our self-assembled arrays with 60-nm-diameter Au nanoparticles perform similarly to lithographically produced sensor substrates.

Another important parameter for sensing is the signal strength, that can be characterized by the peak scattering efficiency Q_{max}. Despite a considerable scatter in Q_{max} values (Figure 7c), most likely caused by variations of NP loading density, the samples with 60 and 80 nm Au NPA have a clear maximum Q_{max} value at wavelengths near λ = 580 nm, which corresponds to h_{PAAO} = 350 nm. A series with finer steps of PAAO thickness variation confirmed the Q_{max} peak wavelength in air λ_{max} = 580 nm (Figure S4a). The $Q_{max}(\lambda_{max})$ peak increased in amplitude and shifted toward longer wavelengths in media with increasing RI. The measurements on 40 nm Au NPA showed a relatively weak scattering. In this case, Q_{max} had linearly increasing dependence on h_{PAAO}. However, suitable scattering peaks could be found only in a comparatively narrow thickness range of ∼350−550 nm (Figure 7c), which explains their absence in earlier experiments.[5] Furthermore, the 40 nm Au NPA scattering had the largest peak width, which reduced the FoM to below 1.

The peak widths (Figure 7d) for Au particles agreed well with simulated data,[14] where full width at half maximum (FWHM) values in the ∼75−100 interval are predicted for individual spherical NPs. However, for Ag NPs, the peaks are notably broader than the calculated values for a single particle. Spectral broadening of scattered light by similar systems (short Ag nanorods embedded in PAAO) has been observed previously and explained by electromagnetic coupling between particles in a dense 2D array.[22] The increased peak width may also be caused by the inhomogeneous broadening due to small changes in size and shape of the Ag nanoparticles.[23]

FDTD simulations were able to qualitatively capture the behavior in experimental observations. Figure 8a shows combined scattering and reflection spectra by 60 nm diameter Au NPs calculated at different PAAO thicknesses. For all thicknesses, the spectra below $\lambda \sim$ 550 nm were dominated by the TFI reflection maxima and minima. A weaker TFI signal could also be observed experimentally in the dark-field images of PAAO without any metal nanoparticles (Figure 4a) and barely noticed in scattering spectra (Figure S5b−d) from reference PAAO sample on the Al substrate. It can be explained by the Rayleigh scattering from the subwavelength inhomogeneities in the thin film, which in the direction normal to the surface enters a Fabry-Pérot like resonator.[24] Most importantly, in the calculated spectra (Figure 8) at h_{PAAO} = 260

https://doi.org/10.1021/acsomega.2c05305
ACS Omega 2022, 7, 40324−40332

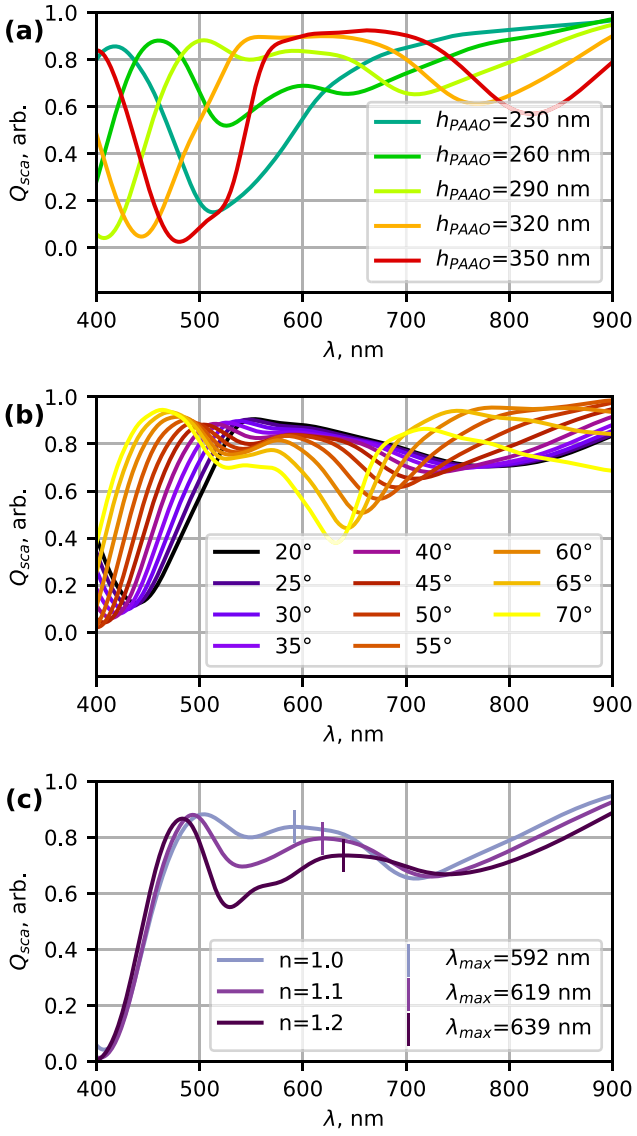

Figure 8. Simulated spectra of 60 nm Au nanoparticles (a) on various thickness h_{PAAO} layers at a $\theta = 45°$ incidence angle in medium with $n = 1$, (b) on a fixed thickness $h_{PAAO} = 290$ nm layer at different angles and $n = 1$, (c) depending on medium RI, at $\theta = 45°$ and $h_{PAAO} = 290$ nm. Vertical markers indicate the peak wavelength. In all simulations, an s-polarized source was used.

nm, a peak emerged at $\lambda_{max} \sim 600$ nm, which can be attributed to Au nanoparticle LSPR. At higher h_{PAAO}'s, the LSPR peak increased the maximum value and shifted toward longer wavelengths in agreement with the experiment. However, at $h_{PAAO} = 320$ and 350 nm, the peak evolved into a plateau.

An experimental study of the role of the incidence angle is beyond the scope of this article; however, it is an important design consideration for practical sensor devices. For instance, the simulations at a selected thickness $h_{PAAO} = 290$ nm produced observable LSPR peaks near $\lambda_{max} \sim 600$ nm at incidence angles in the 45−65° range (Figure 8b). The actual angle of 60° used in the experiment falls within that range.

Finally, the simulated spectra in different media (Figure 8c) showed a red-shift of LSPR peak wavelength at increased RI values with $\Delta\lambda/\Delta n = 235$, which is close to the highest experimentally measured sensitivity values (Figure 7a and Figure S4a). The LSPR peak width in simulations of ∼100 nm is similar to experimentally observed values (Figure 7d). The simulated TFI peak wavelength $\lambda_{max} \sim 500$ nm in Figure 8c had a relatively small blue-shift in response to increased RI.

The numerical simulations did not take into account several experimental details, in particular, (i) the PAAO pores only locally appear periodic but in practice have a type of short-range ordering (SRO),[3] and (ii) the scattered signal was collected in a solid angle as defined by the numerical aperture (NA) of the objective lens. These two considerations together with the assumption that the Al surface forms a mirror image of nanoparticles (Figure 2) can provide an intuitive understanding of the experimental results. Due to the SRO in lateral dimensions, there is no periodicity on the optical wavelength scale that would lead to constructive interference in any particular direction. However, in the direction normal to the sample surface, all individual particles have a corresponding image particle at exactly the same distance. For s-polarized incidence, the induced dipole moment for each particle would be parallel to the surface, and the image dipole would point in the opposite direction.[18] The particle-image pairs at specific distance and wavelength combinations form a directional antenna[25] with a radiation pattern that fits within the NA of the objective lens. If the wavelength matches the LSPR, this leads to increased Q_{max} values as observed in Figure 7c and Figure S4a. The observed net shift of the peak wavelength depending on h_{PAAO} is a combination of TFI and electromagnetic coupling between LSPR resonators and their mirror images.[26]

Similar MIM systems (Au/Ag nanodisks or hemispheres on Ag mirror separated by Al_2O_3 or SiO_2 spacer) have been discussed using Fano resonances.[27−29] The calculated spectra of the first order scattering by Ag heptamers at spacer distances 300−400 nm from the mirror by Zhu et al.[27] have similar behavior (distinct maximum and red-shift of the peak wavelength with increased spacer thickness) to the first order scattering by 60 and 80 nm NPA in this study. Although we do not observe the typical Fano line shapes, the coupling between Au NPs and the Al surface or mirror NPs may contribute to the asymmetry of scattering spectra and modulate the RI sensitivity.

3. CONCLUSIONS

Using capillary force assisted colloidal nanoparticle deposition on PAAO templates on an Al substrate, we have produced non-close-packed arrays with a high density of ∼100 μm^{-2} and demonstrated their use for refractometric sensing. A convenient, fast, and nondestructive all-optical method for finding the PAAO thickness for the best sensitivity or best signal intensity was developed. The highest RI sensitivity was found for 60 nm Au NPs on PAAO with an effective thickness of approximately 500 nm and exceeded 200 nm/RIU. For the highest signal to background ratio, the NP with 60 and 80 nm diameter on 350 nm thick PAAO were most suitable. The 40 nm Au NP had the least favorable performance in terms of signal strength, usable PAAO thickness range, and FoM. The sensitivity of the PAAO-Au NP sensors was similar to single-particle devices reported in the literature, but the high-density MIM structures presented here have the advantage of scattering signal gain, which can be attributed to the constructive interference between radiation by nanoparticles and their mirror images.

FDTD simulations on 60 nm Au NPs estimated the RI sensitivity to 235 nm/RIU, which is close to the highest

https://doi.org/10.1021/acsomega.2c05305
ACS Omega 2022, 7, 40324−40332

measured value. Simulations showed that the angle of incidence can potentially be used to improve the detection at certain PAAO thicknesses.

4. METHODS

4.1. Experiment. Continuous thickness-gradient PAAO films were produced by two step anodization of high-purity (99.999%) aluminum sheets (GoodFellow AL000637, CAS: 7429-90-5) in 0.3 M $C_2H_2O_4$ (oxalic acid 98% Sigma-Aldrich 194131, CAS: 144-62-7) electrolyte with a 40 V anodizing voltage.[30] During the second anodization, the Al sheets were gradually pulled out of the electrolyte at a 4.6 mm/min rate. This resulted in an approximately 100-nm- to 1-μm-thick PAAO wedge over a 1 cm distance, pore diameters 30−35 nm, and a center-to-center distance of 100 nm. Full details are available elsewhere.[31]

Fixed-thickness PAAO films were produced on single crystal <100> aluminum substrates (MTI Corp. mcALa101010) for reference measurements. The effective thickness h_{PAAO} of the aluminum oxide layer was determined by reflectance spectroscopy measurements and fitting the spectra to a transfer-matrix multilayer model,[16] which consisted of a substrate with a complex refractive index $n + ik$ for aluminum[32] and a layer of aluminum oxide with an effective refractive index $n_{eff,PAAO}$ = 1.6. This value gives a good agreement between optical and SEM measurement of PAAO thickness.[33] It should be noted that the effective thickness h_{PAAO} accommodates the subwavelength inhomogeneities of PAAO, such as barrier layer, voids (pores), and funnel-shaped pore openings.

Dense NCP arrays were produced by dip-coating the variable thickness PAAO in Au nanoparticle suspensions with different particle diameters: 40 nm, Sigma-Aldrich 753637, absorption λ_{max} 529−533 nm; 60 nm, Sigma-Aldrich 753653, λ_{max} 538−544 nm; 80 nm, Sigma-Aldrich 753661, λ_{max} 550−557 nm. The withdrawal direction y was perpendicular to PAAO thickness gradient direction x (Figure S2). The withdrawal speed was repeatedly varied from 2 μm/s to 0.5 μm/s and 0.1 μm/s resulting in ∼1 mm broad zones with different loading densities.[5] 1:1 scale macroscopic photographs of samples are shown in Figure S2, whereas Figure 4a shows dark-field microscope images of selected high loading density zones. For comparison, 60 nm Ag nanoparticles (Sigma-Aldrich 730815, λ_{max} 425−450 nm) were also deposited. Sparse NPAs on fixed-thickness-PAAO were produced by drop casting 20 μL of 60 nm Au suspension. After drying in air (overnight), the residues of salts from PBS were dissolved in water.

Figure 2 shows the optical configuration of the benchmarking setup. Samples were illuminated by a collimated and polarized beam of light from a halogen lamp (THORLABS OSL1). The scattered light intensity $I(\lambda)$ was collected though a microscope lens (40×, NA 0.6, Olympus) and analyzed with a fiber-coupled spectrometer (Ocean Optics USB4000). Here, λ is the wavelength of the incidence radiation. Initially, the gap between the NPA and a standard microscope glass slide was filled with air (n = 1). For each sample, a series of spectra together with lateral coordinates was recorded from spots with different thicknesses h_{PAAO}. Thereafter, the gap was filled with water (Sigma-Aldrich 38796, CAS: 7732-18-5), and spectra were recorded at the same spots with coordinates set by the programmable motorized microscope stage (PRIOR). Finally, spectra from the same spots were recorded using a sucrose (CAS: 57-50-1, Enola, for cell culture) 40 wt % solution. Reflectance from the aluminum mirror (Thorlabs PF05−03-G01) was used as a white reference spectrum $R(\lambda)$.

The scattering efficiency $Q_{sca}(\lambda) = I(\lambda)/R(\lambda)$ recorded in different media was used to calculate the RI sensitivity $S = \Delta\lambda/\Delta n$, where $\Delta\lambda$ is the difference between peak wavelengths of $Q_{sca}(\lambda)$ in respective media with RI difference Δn. The efficiency peak wavelengths λ_{max} were found by approximating the $Q_{sca}(\lambda)$ with a 10th order polynomial and finding its maximum in the 450−800 nm wavelength range. Since the spectral peaks were asymmetrical and the baseline estimates could be ambiguous, the wavelength difference W between inflection points on both sides of polynomial maxima served as the FWHM value for calculation of the figure of merit (FoM = S/FWHM).

4.2. Simulations. Numerical simulations of corresponding structures were done using the finite-difference time-domain (FDTD) software (Ansys-Lumerical, version 2021 R2.3). The model structure consisted of an aluminum substrate, an aluminum oxide layer with cylindrical pores (PAAO), and gold nanoparticles. The thickness of the PAAO layer was varied from 230 to 350 nm in steps of 30 nm. The pore diameter was 35 nm, and the distance between the pore centers was 100 nm. 60-nm-diameter gold nanoparticles were placed directly above each pore. The built-in materials database was used for the dielectric functions of Al[34] (Palik), Al_2O_3 (Palik), and Au[35] (Johnson and Christy). The refractive index of the surrounding medium was 1, 1.1, and 1.2. The simulation region started 300 nm below the substrate/PAAO interface and ended 1.3 μm above the PAAO surface, while the x and y spans were equal to one period of the structure. The mesh override region ranged from 50 nm below the PAAO to 50 nm above the nanoparticles with a step size in each direction of 2 nm. The broadband fixed angle source technique (BFAST) plane wave light source was placed 500 nm above PAAO with an angle of incidence of 45° and a wavelength range of 300−1000 nm. In some cases, the angle of incidence was varied in the 20−70° range. The frequency domain field and power monitor was placed 1 μm above PAAO to register light after its interaction with a sample.

■ ASSOCIATED CONTENT

Supporting Information

The Supporting Information is available free of charge at https://pubs.acs.org/doi/10.1021/acsomega.2c05305.

SEM image, sample photographs, supplementary measurements of RI sensitivity using 60 nm diameter Au nanoparticles on variable thickness PAAO obtained with a different set of materials and spectroscopy equipment, spectra from the reference sample without nanoparticles (PDF)

■ AUTHOR INFORMATION

Corresponding Author

Juris Prikulis − *Institute of Chemical Physics, University of Latvia, Riga LV-1586, Latvia; Faculty of Physics, Mathematics, and Optometry, University of Latvia, Riga LV-1004, Latvia;* orcid.org/0000-0003-3942-5965; Email: Juris.Prikulis@lu.lv

Authors

Uldis Malinovskis − *Institute of Chemical Physics, University of Latvia, Riga LV-1586, Latvia*

https://doi.org/10.1021/acsomega.2c05305
ACS Omega 2022, 7, 40324−40332

Raimonds Popļausks − *Institute of Chemical Physics, University of Latvia, Riga LV-1586, Latvia*
Aušrinė Jurkevičiūtė − *Institute of Chemical Physics, University of Latvia, Riga LV-1586, Latvia;* orcid.org/0000-0002-8115-5295
Aleksandrs Dutovs − *Institute of Chemical Physics, University of Latvia, Riga LV-1586, Latvia;* orcid.org/0000-0002-3619-6063
Karlis Berzins − *Institute of Chemical Physics, University of Latvia, Riga LV-1586, Latvia*
Vladislavs Perkanuks − *Institute of Chemical Physics, University of Latvia, Riga LV-1586, Latvia*
Wojciech Simka − *Faculty of Chemistry, Silesian University of Technology, 44-100 Gliwice, Poland;* orcid.org/0000-0002-2648-5523
Indrikis Muiznieks − *Faculty of Biology, University of Latvia, Riga LV-1004, Latvia*
Donats Erts − *Institute of Chemical Physics, University of Latvia, Riga LV-1586, Latvia; Faculty of Chemistry, University of Latvia, Riga LV-1586, Latvia;* orcid.org/0000-0003-0345-8845

Complete contact information is available at: https://pubs.acs.org/10.1021/acsomega.2c05305

Notes

The authors declare no competing financial interest.

■ ACKNOWLEDGMENTS

The work was performed within the Latvian Council of Science fundamental and applied research project LZP-2020/1-0200 "Nanostructured multilayer hybrid coatings for interferometric and optoelectronic sensors" and the European Union's Horizon 2020 research and innovation program under grant agreement no. 778157, "Novel 1D photonic metal oxide nanostructures for early stage cancer detection - CanBioSe". A.J. acknowledges postdoctoral research support project no. 1.1.1.2/VIAA/4/20/615. U.M. acknowledges support from ESF project 8.2.2.0/20/I/006. We thank Daniels Jevdokimovs and Kārlis Lazdovskis for the assistance in experiments.

■ REFERENCES

(1) Estevez, M.-C.; Otte, M. A.; Sepulveda, B.; Lechuga, L. M. Trends and challenges of refractometric nanoplasmonic biosensors: A review. *Anal. Chim. Acta* **2014**, *806*, 55−73.
(2) Liu, S.; Tian, J.; Zhang, W. Fabrication and application of nanoporous anodic aluminum oxide: a review. *Nanotechnology* **2021**, *32*, 222001.
(3) Malinovskis, U.; Poplausks, R.; Apsite, I.; Meija, R.; Prikulis, J.; Lombardi, F.; Erts, D. Ultrathin Anodic Aluminum Oxide Membranes for Production of Dense Sub-20 nm Nanoparticle Arrays. *J. Phys. Chem. C* **2014**, *118*, 8685−8690.
(4) Malinovskis, U.; Berzins, A.; Gahbauer, F.; Ferber, R.; Kitenbergs, G.; Muiznieks, I.; Erts, D.; Prikulis, J. Colloidal nanoparticle sorting and ordering on anodic alumina patterned surfaces using templated capillary force assembly. *Surf. Coat. Technol.* **2017**, *326*, 264−269.
(5) Malinovskis, U.; Poplausks, R.; Erts, D.; Ramser, K.; Tamulevičius, S.; Tamulevičienė, A.; Gu, Y.; Prikulis, J. High-Density Plasmonic Nanoparticle Arrays Deposited on Nanoporous Anodic Alumina Templates for Optical Sensor Applications. *Nanomaterials* **2019**, *9*, 531.
(6) Jiang, W.; Ma, Y.; Zhao, J.; Li, L.; Xu, Y.; Guo, H.; Song, L.; Chen, Z.; Zhang, Y. Robust Assembly of Colloidal Nanoparticles for Controlled-Reflectance Surface Construction. *ACS Appl. Mater. Interfaces* **2019**, *11*, 23773−23779.
(7) Wu, X.-X.; Jiang, W.-Y.; Wang, X.-F.; Zhao, L.-Y.; Shi, J.; Zhang, S.; Sui, X.; Chen, Z.-X.; Du, W.-N.; Shi, J.-W.; Liu, Q.; Zhang, Q.; Zhang, Y.; Liu, X.-F. Inch-Scale Ball-in-Bowl Plasmonic Nanostructure Arrays for Polarization-Independent Second-Harmonic Generation. *ACS Nano* **2021**, *15*, 1291−1300.
(8) Siegfried, T.; Ekinci, Y.; Martin, O. J.; Sigg, H. Engineering Metal Adhesion Layers That Do Not Deteriorate Plasmon Resonances. *ACS Nano* **2013**, *7*, 2751−2757.
(9) Sekiguchi, K.; Katsumata, K.-i.; Segawa, H.; Nakanishi, T.; Yasumori, A. Effects of particle size, concentration and pore size on the loading density of silica nanoparticle monolayer arrays on anodic aluminum oxide substrates prepared by the spin-coating method. *Mater. Chem. Phys.* **2022**, *277*, 125465.
(10) Sulka, G. D. *Nanostructured Materials in Electrochemistry*; Wiley-VCH Verlag GmbH & Co. KGaA: Weinheim, Germany, 2008; pp 1−116.
(11) O'Sullivan, J. P.; Wood, G. C. The morphology and mechanism of formation of porous anodic films on aluminium. *Proc. R. Soc. London A* **1970**, *317*, 511−543.
(12) Fritzsche, J.; Albinsson, D.; Fritzsche, M.; Antosiewicz, T. J.; Westerlund, F.; Langhammer, C. Single Particle Nanoplasmonic Sensing in Individual Nanofluidic Channels. *Nano Lett.* **2016**, *16*, 7857−7864.
(13) Chen, H.; Kou, X.; Yang, Z.; Ni, W.; Wang, J. Shape- and Size-Dependent Refractive Index Sensitivity of Gold Nanoparticles. *Langmuir* **2008**, *24*, 5233−5237.
(14) Singh Sekhon, J.; S Verma, S. Refractive Index Sensitivity Analysis of Ag, Au, and Cu Nanoparticles. *Plasmonics* **2011**, *6*, 311−317.
(15) Mino, Y.; Watanabe, S.; Miyahara, M. T. In Situ Observation of Meniscus Shape Deformation with Colloidal Stripe Pattern Formation in Convective Self-Assembly. *Langmuir* **2015**, *31*, 4121−4128.
(16) Prikulis, J.; Tamulevičius, T.; Poplausks, R.; Bergs, G.; Apsite, I.; Malinovskis, U.; Actins, A.; Erts, D. Optical properties of thin metal films with nanohole arrays on porous alumina-aluminum structures. *RSC Adv.* **2015**, *5*, 68143−68150.
(17) Prikulis, J.; Malinovskis, U.; Poplausks, R.; Apsite, I.; Bergs, G.; Erts, D. Optical Scattering by Dense Disordered Metal Nanoparticle Arrays. *Plasmonics* **2014**, *9*, 427−434.
(18) Li, X.; Arnoldus, H. F. Electric dipole radiation near a mirror. *Phys. Rev. A* **2010**, *81*, 053844.
(19) Manzano, C. V.; Ramos, D.; Pethö, L.; Bürki, G.; Michler, J.; Philippe, L. Controlling the Color and Effective Refractive Index of Metal-Anodic Aluminum Oxide (AAO)-Al Nanostructures: Morphology of AAO. *J. Phys. Chem. C* **2018**, *122*, 957−963.
(20) Bonyár, A. Maximizing the Surface Sensitivity of LSPR Biosensors through Plasmon Coupling-Interparticle Gap Optimization for Dimers Using Computational Simulations. *Biosensors* **2021**, *11*, 527.
(21) Piliarik, M.; Kvasnička, P.; Galler, N.; Krenn, J. R.; Homola, J. Local refractive index sensitivity of plasmonic nanoparticles. *Opt. Express* **2011**, *19*, 9213.
(22) Biring, S.; Wang, H.-H.; Wang, J.-K.; Wang, Y.-L. Light scattering from 2D arrays of monodispersed Ag-nanoparticles separated by tunable nano-gaps: spectral evolution and analytical analysis of plasmonic coupling. *Opt. Express* **2008**, *16*, 15312.
(23) Billaud, P.; Huntzinger, J.-R.; Cottancin, E.; Lermé, J.; Pellarin, M.; Arnaud, L.; Broyer, M.; Del Fatti, N.; Vallée, F. Optical extinction spectroscopy of single silver nanoparticles. *Eur. Phys. J. D* **2007**, *43*, 271−274.
(24) Akalin, T.; Danglot, J.; Vanbesien, O.; Lippens, D. A highly directive dipole antenna embedded in a Fabry-Perot type cavity. *IEEE Microw. Wirel. Components Lett.* **2002**, *12*, 48−50.
(25) Munárriz, J.; Malyshev, A. V.; Malyshev, V. A.; Knoester, J. Optical Nanoantennas with Tunable Radiation Patterns. *Nano Lett.* **2013**, *13*, 444−450.

(26) Benz, F.; de Nijs, B.; Tserkezis, C.; Chikkaraddy, R.; Sigle, D. O.; Pukenas, L.; Evans, S. D.; Aizpurua, J.; Baumberg, J. J. Generalized circuit model for coupled plasmonic systems. *Opt. Express* **2015**, *23*, 33255.
(27) Zhu, X.; Shi, H.; Zhang, S.; Liu, Q.; Duan, H. Constructive-interference-enhanced Fano resonance of silver plasmonic heptamers with a substrate mirror: a numerical study. *Opt. Express* **2017**, *25*, 9938.
(28) Ogier, R.; Shao, L.; Svedendahl, M.; Käll, M. Continuous-Gradient Plasmonic Nanostructures Fabricated by Evaporation on a Partially Exposed Rotating Substrate. *Adv. Mater.* **2016**, *28*, 4658−4664.
(29) Okamoto, K.; Okura, K.; Wang, P.; Ryuzaki, S.; Tamada, K. Flexibly tunable surface plasmon resonance by strong mode coupling using a random metal nanohemisphere on mirror. *Nanophotonics* **2020**, *9*, 3409−3418.
(30) Masuda, H.; Fukuda, K. Ordered Metal Nanohole Arrays Made by a Two-Step Replication of Honeycomb Structures of Anodic Alumina. *Science* **1995**, *268*, 1466−1468.
(31) Poplausks, R.; Jevdokimovs, D.; Malinovskis, U.; Erts, D.; Prikulis, J. Variable Thickness Porous Anodic Alumina/Metal Film Bilayers for Optimization of Plasmonic Scattering by Nanoholes on Mirror. *ACS Omega* **2018**, *3*, 5783−5788.
(32) Rakić, A. D.; Djurišić, A. B.; Elazar, J. M.; Majewski, M. L. Optical properties of metallic films for vertical-cavity optoelectronic devices. *Appl. Opt.* **1998**, *37*, 5271.
(33) Malinovskis, U.; Dutovs, A.; Poplausks, R.; Jevdokimovs, D.; Graniel, O.; Bechelany, M.; Muiznieks, I.; Erts, D.; Prikulis, J. Visible Photoluminescence of Variable-Length Zinc Oxide Nanorods Embedded in Porous Anodic Alumina Template for Biosensor Applications. *Coatings* **2021**, *11*, 756.
(34) Palik, E. D. *Handbook of Optical Constants of Solids*; Academic Press: New York, 1997.
(35) Johnson, P. B.; Christy, R. W. Optical Constants of the Noble Metals. *Phys. Rev. B* **1972**, *6*, 4370−4379.

https://doi.org/10.1021/acsomega.2c05305
ACS Omega 2022, 7, 40324−40332